Eur. Phys. J. A **30**, 141–151 (2006)
DOI 10.1140/epja/i2006-10112-y

THE EUROPEAN PHYSICAL JOURNAL A

Instabilities in nuclear matter and finite nuclei

V. Baran[1,a] and J. Margueron[2]

[1] Physics Faculty, Bucharest University and IFIN-HH Bucharest, Romania
[2] Institut de Physique Nucléaire, Université Paris Sud F-91406 Orsay CEDEX, France

Received: 16 June 2006 /
Published online: 31 October 2006 – © Società Italiana di Fisica / Springer-Verlag 2006

Abstract. Spinodal instability in nuclear matter and finite nuclei is investigated. This instability occurs in the low-density region of the phase diagram. The thermodynamical and dynamical analysis is based on Landau theory of Fermi liquids. It is shown that asymmetric nuclear matter can be characterized by a unique spinodal region, defined by the instability against isoscalar-like fluctuation, as in symmetric nuclear matter. Everywhere in this density region the system is stable against isovector-like fluctuations related to the species separation tendency. Nevertheless, this instability in asymmetric nuclear matter induces isospin distillation leading to a more symmetric liquid phase and a more neutron-rich gas phase.

PACS. 21.65.+f Nuclear matter – 25.70.Pq Multifragment emission and correlations – 21.60.Ev Collective models

1 Introduction

The production of fragments represents an important dissipation mechanism in heavy-ion reactions at intermediate energies. A relevant phenomenon is the liquid-gas phase transition, very often invoked in discussing the nuclear multifragmentation. In this analogy, however, one should be aware also of the differences due to Coulomb, finite-size or quantum effects.

For phase transitions in macroscopic systems, the coexistence regions, corresponding to areas thermodynamically forbidden for one single phase, exhibit general features such as metastabilities or instabilities. At variance with the situation for macroscopic systems, where the observation time scale is much greater than the time scales of the microscopic processes that lead to drop (bubble) formation (even more exceptional is the study of critical points where the slowing-down phenomena require days of expectations for equilibration), in heavy-ions collisions the reaction times can be comparable to the fragment formation time which is of relevance for discussing about the kinetics of the phase transition. The violent collision and fast expansion may quench the system inside the instability region of the phase diagram. Moreover, a binary system, including asymmetric nuclear matter (ANM) (see [1]), manifest a richer thermodynamical behaviour, since it has to accommodate one more conservation law.

In this paper we will discuss first the nature of the instabilities and of the related fluctuations in such systems. Then, in sect. 3, we will describe the kinetics of phase transition in ANM both in the linear and nonlinear regime. Finally, in the last section we will focus on the relevance of these results on nuclear multifragmentation and neck fragmentation in heavy-ion collisions at intermediate energies.

[a] e-mail: baran@lns.infn.it

2 Instabilities and fluctuations in ANM

2.1 Thermodynamical approach

One-component systems may become unstable against density fluctuations as the result of the mean attractive interaction between constituents. In symmetric binary systems, like symmetric nuclear matter (SNM), one may encounter two kinds of density fluctuations: i) isoscalar, when the densities of the two components oscillate in phase with equal amplitude, ii) isovector when the two densities fluctuate still with equal amplitude but out of phase. Then mechanical instability is associated with instability against isoscalar fluctuations leading to cluster formation while chemical instability is related to instability against isovector fluctuations, leading to species separation. We will show in the following that in ANM, there is no longer a one-to-one correspondence between isoscalar (respectively isovector) fluctuations and mechanical (respectively chemical) instability. An appropriate framework for the study of instabilities is provided by the Fermi-liquid theory [2], which has been applied, for instance, to symmetric binary systems as SNM (the two components being protons and neutrons) [3], the liquid ^{3}He (spin-up

and spin-down components) [4,5] and proto-neutron stars to calculate neutrino propagation [6].

The starting point is an extension to the asymmetric case of the formalism introduced in [4]. The distribution functions for protons and neutrons are

$$f_q\big(\epsilon_p^q\big) = \Theta\big(\mu_q - \epsilon_p^q\big), \qquad q = n, p, \tag{1}$$

where μ_q are the corresponding chemical potentials. The nucleon interaction is characterized by the Landau parameters:

$$F^{q_1 q_2} = N_{q_1} V^2 \frac{\delta^2 H}{\delta f_{q_1} \delta f_{q_2}} = N_{q_1} \frac{\delta^2 H}{\delta \rho_{q_1} \delta \rho_{q_2}}\,, \tag{2}$$

$$N_q(T) = \int \frac{-2\,\mathrm{d}\mathbf{p}}{(2\pi\hbar)^3} \frac{\partial f_q(T)}{\partial \epsilon_p^q}\,, \tag{3}$$

where H is the energy density, V is the volume and N_q is the single-particle level density at the Fermi energy. At $T = 0$ this reduces to

$$N_q(0) = m p_{F,q} / \big(\pi^2 \hbar^3\big) = 3\rho_q / \big(2\epsilon_{F,q}\big),$$

where $p_{F,q}$ and $\epsilon_{F,q}$ are the Fermi momentum and Fermi energy of the q-component. Thermodynamical stability for $T = 0$ requires the energy of the system to be an absolute minimum for the undistorted distribution functions, so that the relation

$$\delta H - \mu_p \delta\rho_p - \mu_n \delta\rho_n > 0 \tag{4}$$

is satisfied when we deform proton and neutron Fermi seas.

Only monopolar deformations will be taken into account, since we consider here momentum-independent interactions, so that $F_{l=0}^{q_1 q_2}$ are the only non-zero Landau parameters. In fact, for momentum-independent interactions, all the information on all possible instabilities of the system is obtained just considering density variations. However, one should keep in mind that in the actual dynamical evolution of an unstable system in general one observes deformations of the Fermi sphere, hence the direction taken by the system in the dynamical evolution is not necessarily the most unstable one defined by the thermodynamical analysis.

Then, up to second order in the variations, the condition eq. (4) becomes

$$\delta H - \mu_p \delta\rho_p - \mu_n \delta\rho_n = \frac{1}{2}\big(a\delta{\rho_p}^2 + b\delta{\rho_n}^2 + c\delta\rho_p\delta\rho_n\big) > 0, \tag{5}$$

where

$$\begin{aligned} &a = N_p(0)(1 + F_0^{pp}); \qquad b = N_n(0)(1 + F_0^{nn}); \\ &c = N_p(0)F_0^{pn} + N_n(0)F_0^{np} = 2N_p(0)F_0^{pn}. \end{aligned} \tag{6}$$

The r.h.s. of eq. (5) is diagonalized by the following transformation:

$$\begin{aligned} u &= \cos\beta\,\delta\rho_p + \sin\beta\,\delta\rho_n, \\ v &= -\sin\beta\,\delta\rho_p + \cos\beta\,\delta\rho_n, \end{aligned} \tag{7}$$

where the *mixing* angle $0 \le \beta \le \pi/2$ is given by

$$tg\,2\beta = \frac{c}{a-b} = \frac{N_p(0)F_0^{pn} + N_n(0)F_0^{np}}{N_p(0)(1+F_0^{pp}) - N_n(0)(1+F_0^{nn})}\,. \tag{8}$$

Then eq. (5) takes the form

$$\delta H - \mu_p \delta\rho_p - \mu_n \delta\rho_n = Xu^2 + Yv^2 > 0, \tag{9}$$

where

$$\begin{aligned} X &= \frac{1}{2}\big(a + b + \mathrm{sign}(c)\sqrt{(a-b)^2 + c^2}\big) \\ &\equiv \frac{(N_p(0) + N_n(0))}{2}\big(1 + F_{0g}^s\big) \end{aligned} \tag{10}$$

and

$$\begin{aligned} Y &= \frac{1}{2}\big(a + b - \mathrm{sign}(c)\sqrt{(a-b)^2 + c^2}\big) \\ &\equiv \frac{(N_p(0) + N_n(0))}{2}\big(1 + F_{0g}^a\big), \end{aligned} \tag{11}$$

defining the new generalized Landau parameters $F_{0g}^{s,a}$.

Hence, thanks to the rotation eq. (7), it is possible to separate the total variation eq. (4) into two independent contributions, called the "normal" modes, and characterized by the "mixing angle" β, which depends on the density of states and the details of the interaction. Thus, the thermodynamical stability requires $X > 0$ and $Y > 0$. Equivalently, the following conditions have to be fulfilled:

$$1 + F_{0g}^s > 0 \quad \text{and} \quad 1 + F_{0g}^a > 0. \tag{12}$$

They represent Migdal-Pomeranchuk stability conditions extended to asymmetric binary systems.

The new stability conditions, eq. (12), are equivalent to mechanical and chemical stability of a thermodynamical state [7], *i.e.*

$$\left(\frac{\partial P}{\partial \rho}\right)_{T,y} > 0 \quad \text{and} \quad \left(\frac{\partial \mu_p}{\partial y}\right)_{T,P} > 0, \tag{13}$$

where P is the pressure and y the proton fraction. In fact, mechanical and chemical stability are very general conditions, deduced by requiring that the principal curvatures of thermodynamical potential surfaces, such as the free energy (or the entropy) with respect to the extensive variables are positive (negative).

It has been argued that the mechanical and chemical instability lead to very different phenomenons: the chemical instability with the concentration as order parameter and the mechanical instability for which the total density plays the role of a second-order parameter [8,9]. In the following, we will show that spinodal instability and phase transition in ANM should be instead discussed in terms of isoscalar- and isovector-like instabilities. In the case discussed here, it can be proved that [10]:

$$\begin{aligned} XY &= N_p(0)N_n(0)\big[(1 + F_0^{nn})(1 + F_0^{pp}) - F_0^{np}F_0^{pn}\big] \\ &= \frac{[N_p(0)N_n(0)]^2}{(1-y)\rho^2} \left(\frac{\partial P}{\partial \rho}\right)_{T,y} \left(\frac{\partial \mu_p}{\partial y}\right)_{T,P} \end{aligned} \tag{14}$$

and

$$\left(\frac{\partial P}{\partial \rho}\right)_{T,y} = \frac{\rho y(1-y)}{N_p(0)N_n(0)}\left(t\,a + \frac{1}{t}\,b + c\right)$$
$$\propto X\left(\sqrt{t}\cos\beta + \frac{1}{\sqrt{t}}\sin\beta\right)^2 + Y\left(\sqrt{t}\sin\beta - \frac{1}{\sqrt{t}}\cos\beta\right)^2$$
$$\text{with} \quad t = \frac{y}{1-y}\frac{N_n(0)}{N_p(0)}\,. \tag{15}$$

Let us assume that in the density range we are considering the quantities a and b remain positive. In this way one can study the effect of the interaction between the two components, given by c, on the instabilities of the mixture. If $c < 0$, *i.e.* for an attractive interaction between the two components, from eq. (11) one sees that the system is stable against isovector-like fluctuations. It becomes isoscalar unstable if $c < -2\sqrt{ab}$ (see eq. (10)). However thermodynamically this instability against isoscalar-like fluctuations will show up as a chemical instability if $(-ta - b/t) < c < -2\sqrt{ab}$ or as a mechanical instability if $c < (-ta - b/t) < -2\sqrt{ab}$ (see eq. (15)). This last observation is very interesting: it tells us that the nature of the thermodynamically instabilities can be related to the relative strength of the various interactions among the species. In other words, if it is possible to determine experimentally for a binary systems the signs of $(\frac{\partial P}{\partial \rho})_{T,y}$ and/or $(\frac{\partial \mu_p}{\partial y})_{T,P}$ we can learn about the inequalities, at a given density, between species interactions.

On the other hand, the distinction between the two kinds of instability (mechanical and chemical) is not really relevant regarding the nature of unstable fluctuations, being it essentially the same, *i.e.* isoscalar-like. The relevant instability region is defined in terms of instabilities against isoscalar fluctuations and we can speak, therefore, about a unique spinodal region. If $c > 0$, *i.e.* when the interaction between the components is repulsive, the thermodynamical state is always stable against isoscalar-like fluctuation, but can be isovector unstable if $c > 2\sqrt{ab}$. Since with our choices the system is mechanically stable ($a, b, c > 0$, see eq. (15)), the isovector instability is now always associated with chemical instability. Such situation will lead to a component separation of the liquid mixture. In this framework, a complete analysis of the instabilities of any binary system can be performed, in connection to signs, strengths and density dependence of the interactions.

2.2 Asymmetric nuclear-matter case

We show now quantitative calculations for asymmetric nuclear matter which illustrate the previous general discussion on instabilities. Let us consider a potential energy density of Skyrme type [11,12],

$$H_{pot}(\rho_n,\rho_p) = \frac{A}{2}\frac{(\rho_n+\rho_p)^2}{\rho_0} + \frac{B}{\alpha+2}\frac{(\rho_n+\rho_p)^{\alpha+2}}{\rho_0^{\alpha+1}}$$
$$+\left(C_1 - C_2\left(\frac{\rho}{\rho_0}\right)^{\alpha}\right)\frac{(\rho_n-\rho_p)^2}{\rho_0}\,, \tag{16}$$

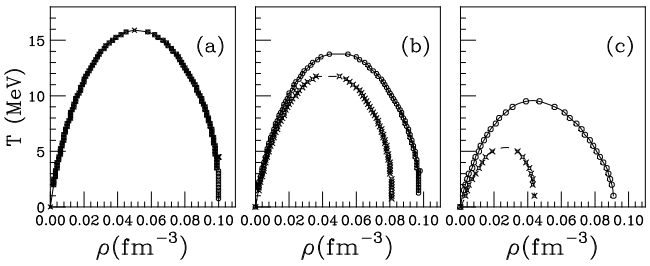

Fig. 1. Spinodal line corresponding to isoscalar-like instability of asymmetric nuclear matter (circles) and mechanical instability (crosses) for three proton fractions: $y = 0.5$ (a), $y = 0.25$ (b), $y = 0.1$ (c). The figure is taken from [10].

where $\rho_0 = 0.16\,\mathrm{fm}^{-3}$ is the nuclear saturation density. The values of the parameters $A = -356.8\,\mathrm{MeV}$, $B = 303.9\,\mathrm{MeV}$, $\alpha = 1/6$, $C_1 = 125\,\mathrm{MeV}$, $C_2 = 93.5\,\mathrm{MeV}$ are adjusted to reproduce the saturation properties of symmetric nuclear matter and the symmetry energy coefficient.

We focus on the low-density region, where phase transitions of the liquid-gas type are expected to happen, in agreement with the experimental evidences of multifragmentation [13,14]. Since $a, b > 0$ and $c < 0$, we deal only with instability against isoscalar-like fluctuations, as for symmetric nuclear matter. In fig. 1 the circles represent the spinodal line corresponding to isoscalar-like instability, as defined above, for three values of the proton fraction. For asymmetric matter, $y < 0.5$, under this border one encounters either chemical instability, in the region between the two lines, or mechanical instability, under the inner line (crosses). The latter is defined by the set of values (ρ, T) for which $(\frac{\partial P}{\partial \rho})_{T,y} = 0$. We observe that the line defining chemical instability is more robust against the variation of the proton fraction in comparison to that defining mechanical instability: reducing the proton fraction makes it energetically less and less favorable for the system to break into clusters with the same initial asymmetry. However, we stress again the unique nature of the isoscalar-like instability. The change from the chemical to the mechanical character along this border line is not very meaningful and does not affect the properties of the system.

Let us now discuss the generality of the conclusions by comparing several models for the nuclear interaction. Indeed, the spinodal contours predicted by several models exhibit important differences (see fig. 2). In the case of SLy230a force (as well as SGII, D1P), the total density at which spinodal instability appears decreases when the asymmetry increases whereas for SIII (as well as D1, D1S) it increases up to large asymmetry and finally decreases. Despite the observed differences between the models, we observe that all forces which fulfill the global requirement that they reproduce the symmetric nuclear-matter (SNM) equation of state as well as the pure neutron matter calculations lead to the same curvature of the spinodal region [15].

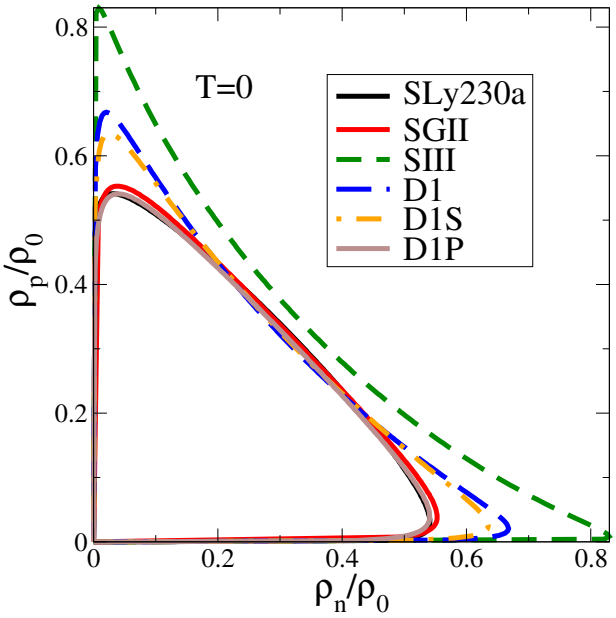

Fig. 2. Projection of the spinodal contour in the density plane for several effective interactions like Skyrme (SLy230a, SGII, SIII) and Gogny (D1, D1S, D1P). The figure is taken from [15].

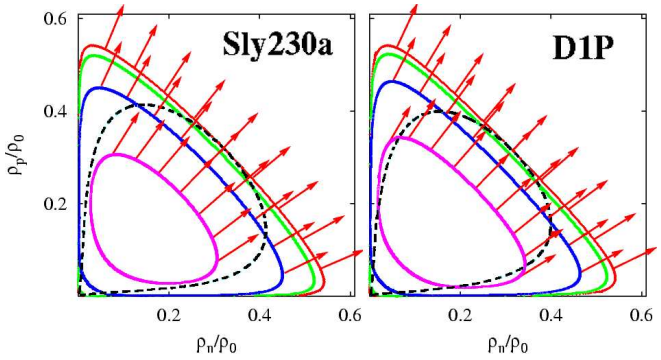

Fig. 3. Projection of the iso-eigen values on the density plane for Slya (left) and D1P (right). The arrows indicate the direction of instability. The mechanical instability is also indicated (dashed line). The figure is taken from [15].

Let us now focus on the direction of the instability. If the eigenvector associated with the unstable mode is along $y = \rho_p/\rho = \text{const}$ then the instability does not change the proton fraction. For symmetry reasons pure isoscalar and isovector modes appear only for SNM so it is interesting to introduce a generalization of isoscalar-like and isovector-like modes by considering if the protons and neutrons move in phase ($\delta\rho_n\delta\rho_p > 0$) or out of phase ($\delta\rho_n\delta\rho_p < 0$). Figure 3 shows the direction of instabilities along the spinodal border and some iso-instability lines. We observe that instability is always almost along the ρ-axis meaning that it is dominated by total density fluctuations even for large asymmetries. The instability direction is between the $y = \text{const}$ line and the ρ-direction. This shows that the unstable direction is of isoscalar nature as expected from the attractive proton-neutron interaction. The total density is, therefore, the dominant contribution to the order parameter showing that the transition is between two phases having different densities (*i.e.* liquid-gas phase transition). The angle with the ρ-axis is almost constant along a constant y line. This means that as the matter enters in the spinodal zone and then dives into it, there are no dramatic changes in the instability direction which remains essentially a density fluctuation. Moreover, the unstable eigenvector drives the dense phase (*i.e.* the liquid) toward a more symmetric point in the density plane. By particle conservation, the gas phase will be more asymmetric leading to the fractionation phenomenon.

We want to stress that those qualitative conclusions are very robust and have been reached for all the Skyrme and Gogny forces we have tested (SGII, SkM*, RATP, D1, D1S, D1P) including the most recent one (SLy230a, D1P) as well as the original one (like SIII, D1).

We eventually point out that also various relativistic mean-field hadron models were involved for the study of the phase transition from liquid to gas phases in ANM [8, 16,17]. It was concluded that the largest differences between different parameterizations, regarding unstable behaviour in the low-density region, occur at finite temperature and in the high isospin asymmetry region.

3 The kinetics of phase transition in ANM

3.1 The linear response

The dynamical behaviour of a two-fluid system can be described, at the semi-classical level, by considering two Vlasov equations, for neutrons and protons in the nuclear-matter case [11,12,18,19], coupled through the self-consistent nuclear field

$$\frac{\partial f_q(\mathbf{r},\mathbf{p},t)}{\partial t}+\frac{\mathbf{p}}{m}\frac{\partial f_q}{\partial \mathbf{r}}-\frac{\partial U_q(\mathbf{r},t)}{\partial \mathbf{r}}\frac{\partial f_q}{\partial \mathbf{p}}=0, \qquad q=n,p. \quad (17)$$

For simplicity effective mass corrections are neglected. In fact, in the low-density region, of interest for our analysis of spinodal instabilities, effective mass corrections should not be large.

$U_q(\mathbf{r},t)$ is the self-consistent mean-field potential in a Skyrme-like form [11,12]:

$$U_q = \frac{\delta H_{pot}}{\delta\rho_q} = A\left(\frac{\rho}{\rho_0}\right)+B\left(\frac{\rho}{\rho_0}\right)^{\alpha+1}+C\left(\frac{\rho_3}{\rho_0}\right)\tau_q + \frac{1}{2}\frac{dC(\rho)}{d\rho}\frac{\rho_3^2}{\rho_0}-D\triangle\rho+D_3\tau_q\triangle\rho_3, \quad (18)$$

where

$$H_{pot}(\rho_n,\rho_p) = \frac{A}{2}\frac{\rho^2}{\rho_0}+\frac{B}{\alpha+2}\frac{\rho^{\alpha+2}}{\rho_0^{\alpha+1}} + \frac{C(\rho)}{2}\frac{\rho_3^2}{\rho_0}+\frac{D}{2}(\nabla\rho)^2-\frac{D_3}{2}(\nabla\rho_3)^2 \quad (19)$$

is the potential energy density (see eq. (16)), where also surface terms are included; $\rho = \rho_n + \rho_p$ and $\rho_3 = \rho_n -$

ρ_p are, respectively, the total (isoscalar) and the relative (isovector) density; $\tau_q = +1$ $(q = n)$, -1 $(q = p)$.

The value of the parameter $D = 130\,\mathrm{MeV}\cdot\mathrm{fm}^5$ is adjusted to reproduce the surface energy coefficient in the Bethe-Weizsäcker mass formula $a_{surf} = 18.6\,\mathrm{MeV}$. The value $D_3 = 40\,\mathrm{MeV}\cdot\mathrm{fm}^5 \sim D/3$ is chosen according to ref. [20], and is also close to the value $D_3 = 34\,\mathrm{MeV}\cdot\mathrm{fm}^5$ given by the SKM* interaction [21].

Let us now discuss the linear response analysis to the Vlasov eqs. (17), corresponding to a semiclassical RPA approach. For a small amplitude perturbation of the distribution functions $f_q(\mathbf{r},\mathbf{p},t)$, periodic in time, $\delta f_q(\mathbf{r},\mathbf{p},t) \sim \exp(-i\omega t)$, eqs. (17) can be linearized leading to the following form:

$$-i\omega\delta f_q + \frac{\mathbf{p}}{m}\frac{\partial\delta f_q}{\partial\mathbf{r}} - \frac{\partial U_q^{(0)}}{\partial\mathbf{r}}\frac{\partial\delta f_q}{\partial\mathbf{p}} - \frac{\partial\delta U_q}{\partial\mathbf{r}}\frac{\partial f_q^{(0)}}{\partial\mathbf{p}} = 0, \quad (20)$$

where the superscript (0) labels stationary values and δU_q is the dynamical component of the mean-field potential. The unperturbed distribution function $f_q^{(0)}$ is a Fermi distribution at finite temperature

$$f_q^{(0)}(\epsilon_p^q) = \frac{1}{\exp\left(\epsilon_p^q - \mu_q\right)/T + 1}\,. \quad (21)$$

Since we are dealing with nuclear matter, $\nabla_r U_q^{(0)} = 0$ in eq. (20) and $\delta f_q \propto \exp(-i\omega t + i\mathbf{kr})$. Following the standard Landau procedure [5,11], one can derive from eqs. (20) the following system of two equations for neutron and proton density perturbations:

$$\left[1 + F_0^{nn}\chi_n\right]\delta\rho_n + \left[F_0^{np}\chi_n\right]\delta\rho_p = 0, \quad (22)$$

$$\left[F_0^{pn}\chi_p\right]\delta\rho_n + \left[1 + F_0^{pp}\chi_p\right]\delta\rho_p = 0, \quad (23)$$

where

$$\chi_q(\omega,\mathbf{k}) = \frac{1}{N_q(T)}\int\frac{2\,\mathrm{d}\mathbf{p}}{(2\pi\hbar)^3}\frac{\mathbf{kv}}{\omega + i0 - \mathbf{kv}}\frac{\partial f_q^{(0)}}{\partial\epsilon_p^q}\,, \quad (24)$$

is the long-wavelength limit of the Lindhard function [5], $\mathbf{v} = \mathbf{p}/m$ and

$$F_0^{q_1q_2}(k) = N_{q_1}(T)\frac{\delta U_{q_1}}{\delta\rho_{q_2}}, \qquad q_1 = n,p, \quad q_2 = n,p \quad (25)$$

are the usual zero-order Landau parameters, as already introduced in eq. (3), where now the k-dependence is due to the presence of space derivatives in the potentials (see eq. (18)). For the particular choice of potentials given by eq. (18), the Landau parameters are expressed as

$$F_0^{q_1q_2}(k) = N_{q_1}(T)\left[\frac{A}{\rho_0} + (\alpha+1)B\frac{\rho^\alpha}{\rho_0^{\alpha+1}} + Dk^2 + \left(\frac{C}{\rho_0} - D'k^2\right)\tau_{q_1}\tau_{q_2} + \frac{\mathrm{d}C}{\mathrm{d}\rho}\frac{\rho'}{\rho_0}(\tau_{q_1}+\tau_{q_2}) + \frac{\mathrm{d}^2C}{\mathrm{d}\rho^2}\frac{\rho'^2}{2\rho_0}\right]. \quad (26)$$

Multiplying the first equation by $N_n^{-1}\chi_p$ and the second one by $N_p^{-1}\chi_n$, we are led to define the following functions:

$$\begin{aligned} a(k,\omega) &= N_p^{-1}\left(1 + F_0^{pp}\chi_p\right)\chi_n;\\ b(k,\omega) &= N_n^{-1}\left(1 + F_0^{nn}\chi_n\right)\chi_p;\\ c(k,\omega) &= \left(N_p^{-1}F_0^{pn} + N_n^{-1}F_0^{np}\right)\chi_n\chi_p = \\ &2N_p^{-1}F_0^{pn}\chi_n\chi_p, \end{aligned} \quad (27)$$

in some analogy with eqs. (6) and we obtain the following system of equations:

$$\begin{aligned} &a\delta\rho_p + c/2\,\delta\rho_n = 0;\\ &c/2\,\delta\rho_p + b\delta\rho_n = 0. \end{aligned} \quad (28)$$

The system can be diagonalized with eigenvalues λ_s and λ_i, solutions of the equation:

$$(a - \lambda_{s,i})(b - \lambda_{s,i}) - c^2/4 = 0.$$

Formally we obtain for $\lambda_{s,i}$ the same expressions as given in eqs. (10), (11) for X and Y, but now a, b and c depend on ω. The unstable solutions for ω are obtained by solving the equations: $\lambda_s = 0$ (for isoscalar-like fluctuations), $\lambda_i = 0$ (for isovector-like fluctuations). This problem is completely equivalent to solve the equation: $c^2(\omega,k) = 4a(\omega,k)b(\omega,k)$, *i.e.* the dispersion relation

$$\left(1 + F_0^{nn}\chi_n\right)\left(1 + F_0^{pp}\chi_p\right) - F_0^{np}F_0^{pn}\chi_n\chi_p = 0, \quad (29)$$

that is also obtained directly by imposing the determinant of the system of eqs. (22), (23) equal to zero.

The dispersion relation is quadratic in ω and one finds two independent solutions (isoscalar-like and isovector-like solutions): ω_s^2 and ω_i^2. Then the structure of the eigenmodes can be determined and one finds

$$\delta\rho_p/\delta\rho_n = -2b(\omega_s,k)/c(\omega_s,k),$$

for the isoscalar-like modes and

$$\delta\rho_p/\delta\rho_n = -2b(\omega_i,k)/c(\omega_i,k),$$

for isovector-like oscillations. However, it is important to notice that the corresponding angles $\beta_{s,i}$ are not equal to the angle β determined in the thermodynamical analysis, eq. (8), because of the ω-dependence in a, b and c. They only coincide with β when $\omega = 0$ (and thus $\chi_{n,p} = 1$), *i.e.* at the border of the unstable region.

The dispersion relation, eq. (29), have been solved for various choices of the initial density, temperature and asymmetry of nuclear matter. Figure 4 reports the growth rate $\Gamma = \mathrm{Im}\,\omega(k)$ as a function of the wave vector k, for three situations inside the spinodal region. Results are shown for symmetric $(I = 0)$ and asymmetric $(I = 0.5)$ nuclear matter.

The growth rate has a maximum $\Gamma_0 = 0.01$–$0.03\,c/\mathrm{fm}$ corresponding to a wave vector value around $k_0 = 0.5$–$1\,\mathrm{fm}^{-1}$ and becomes equal to zero at $k \simeq 1.5k_0$, due to the k-dependence of the Landau parameters, as discussed

above. One can see also that instabilities are reduced when increasing the temperature, an effect also present in the symmetric $N = Z$ case [22–24]. At larger initial asymmetry the development of the spinodal instabilities is slower, the maximum of the growth rate decreases. One should expect also an increase of the size of the produced fragments, decrease of the wave number corresponding to the maximum growth rate. From the long-dashed curves of fig. 4 we can predict the asymmetry effects to be more pronounced at higher temperature, when in fact the system is closer to the boundary of the spinodal region.

A full quantal investigation of spinodal instabilities and the related phase diagram was applied to finite nuclear systems, corresponding to Ca and Sn isotopes [25]. The frequencies and form factors of the unstable collective modes of an excited expanded system were obtained within the linearized time-dependent Hartree-Fock expansion, corresponding to RPA approximation. Dominant features are influenced by the quantum nature of the drop. So the first mode to become unstable is the low-lying octupole vibration. Diluted systems are unstable against low multipole deformations of the surface. It was shown that also in this case the instabilities are mostly of isoscalar nature, with an isovector component leading to isospin distillation, in agreement with the previous predictions for the nuclear-matter case [10].

3.2 Spinodal decomposition: numerical simulations

The previous analytical study is restricted to the onset of fragmentation, and related isospin distillation, in nuclear matter, in a linearized approach. Numerical calculations have been also performed in order to study all stages of the fragment formation process [12,27]. We report on the results of ref. [12] where the same effective Skyrme interactions have been used.

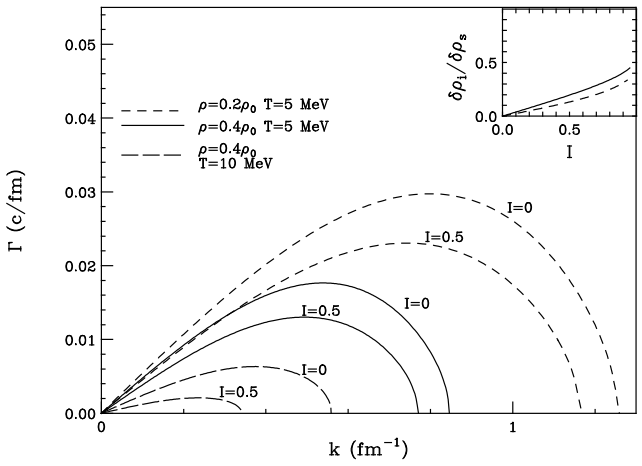

Fig. 4. Growth rates of instabilities as a function of the wave vector, as calculated from the dispersion relation eq. (29), for three situations inside the spinodal region. Lines are labeled with the asymmetry value I. The insert shows the asymmetry of the perturbation $\delta\rho_I/\delta\rho_S$, as a function of the asymmetry I of the initially uniform system, for the most unstable mode, in the case $\rho = 0.4\rho_0$, $T = 5\,\mathrm{MeV}$. The figure is taken from [26].

In the numerical approach the dynamical response of nuclear matter is studied in a cubic box of size L imposing periodic boundary conditions. The Landau-Vlasov dynamics is simulated following a phase-space test particle method, using Gaussian wave packets [28–30]. The dynamics of nucleon-nucleon collisions is included by solving the Boltzmann-Nordheim collision integral using a Monte Carlo method [29]. The width of the Gaussians is chosen in order to correctly reproduce the surface energy value in finite systems. In this way, a cut-off appears in the short-wavelength unstable modes, preventing the formation of too small, unphysical, clusters [22]. The calculations are performed using 80 Gaussians per nucleon and the number of nucleons inside the box is fixed in order to reach the initial uniform density value. An initial temperature is introduced by distributing the test particle momenta according to a Fermi distribution.

We have followed the space-time evolution of test particles in a cubic box with side $L = 24\,\mathrm{fm}$ for three values of the initial asymmetry $I = 0, 0.25$ and 0.5, at initial density $\rho^{(0)} = 0.06\,\mathrm{fm}^{-3} \simeq 0.4\rho_0$ and temperature $T = 5\,\mathrm{MeV}$. The initial density perturbation is created automatically due to the random choice of test particle positions.

The spinodal decomposition mechanism leads to a fast formation of the liquid (high density) and gaseous (low density) phases in the matter. Indeed this dynamical mechanism of clustering will roughly end when the variance saturates [31], *i.e.* around $250\,\mathrm{fm}/c$ in the asymmetric cases. We can also discuss the "chemistry" of the liquid-phase formation. In fig. 5 we report the time evolution of neutron (thick histogram in fig. 5a) and proton (thin histogram in fig. 5a) abundances and of asymmetry (fig. 5b) in various density bins. The dashed lines, respectively, shows the initial uniform density value $\rho \simeq 0.4\rho_0$ (fig. 5a) and the initial asymmetry $I = 0.5$ (fig. 5b). The drive to higher-density regions is clearly different for neutrons and protons: at the end of the dynamical clustering mechanism we have very different asymmetries in the liquid and gas phases (see the panel at $250\,\mathrm{fm}/c$ in fig. 5b).

It was shown in refs. [8,9,20], on the basis of thermodynamics, that the two phases should have different asymmetries, namely, $I_{gas} > I_{liquid}$, and actually a pure neutron gas was predicted at zero temperature if the initial global asymmetry is large enough ($I > 0.4$) [20]. Here we are studying this chemical effect in a non-equilibrium clustering process, on very short time scales, and we confirm the predictions of a linear response approach discussed before.

We can directly check the important result on the unique nature of the most unstable mode, independent of whether we start from a *mechanical* or from a *chemical* instability region. The isospin distillation dynamics presented in fig. 5 refers to the initial conditions of $T = 5\,\mathrm{MeV}$, average density $\rho = 0.06\,\mathrm{fm}^{-3}$ and asymmetry $I = 0.5$, *i.e.* we start from a point well inside the *mechanical* instability region of the used EOS, see fig. 1(b).

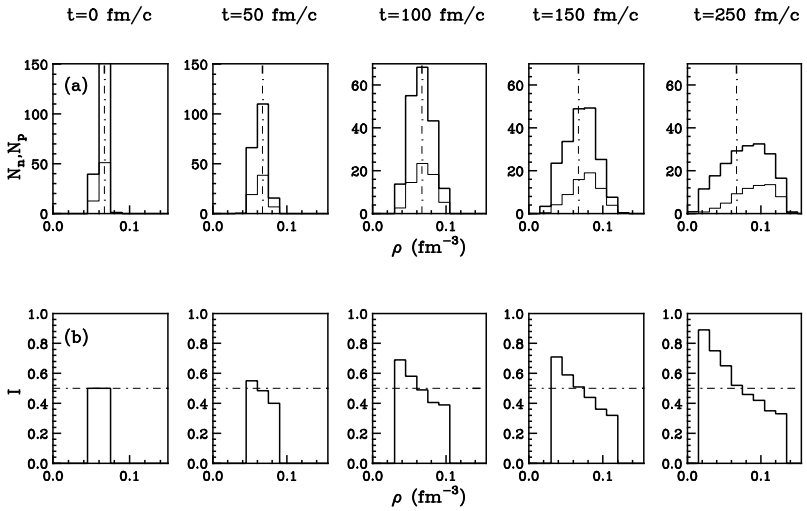

Fig. 5. Time evolution of neutron (thick lines) and proton (thin lines) abundances (a) and of asymmetry (b) in different density bins. The calculation refers to the case of $T = 5\,\mathrm{MeV}$, with initial average density $\rho = 0.06\,\mathrm{fm}^{-3}$ and asymmetry $I = 0.5$ (see the bottom left panel). The figure is taken from [12].

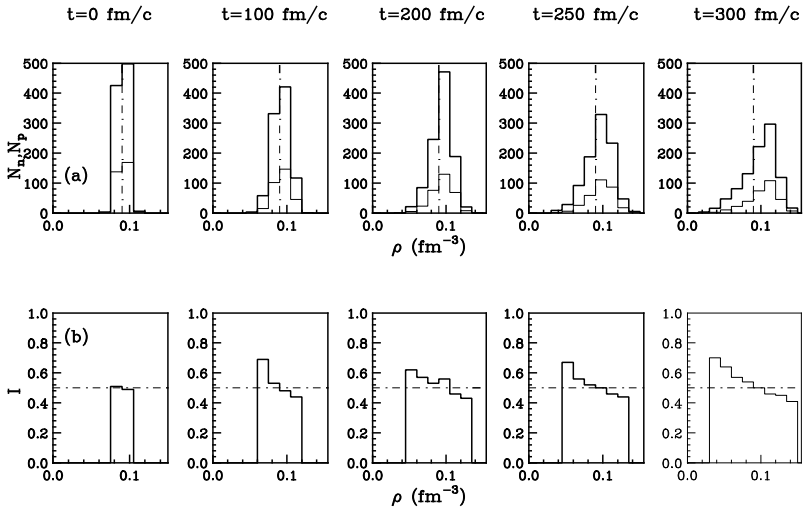

Fig. 6. Same calculation as in fig. 5 but with initial average density $\rho = 0.09\,\mathrm{fm}^{-3}$, inside the *chemical* instability region. The figure is taken from [26].

We can repeat the calculation at the same temperature and initial asymmetry, but starting from an initial average density $\rho = 0.09\,\mathrm{fm}^{-3}$, *i.e.* inside the *chemical* instability region of fig. 1(b). The results for the isospin distillation dynamics are shown in fig. 6. The trend is the same as in the previous fig. 5. This nicely shows the uniqueness of the unstable modes in the spinodal instability region, as discussed in detail in the previous subsection. Such result is due to gross properties of the n/p interaction, thus it should be not dependent on the use of a particular effective force. This has been clearly shown recently in the linear response frame [15], and in full transport simulations [27].

As intuitively expected, and as confirmed by the RPA analysis (see [12]), the isospin distillation effect becomes more important when increasing the initial asymmetry of the system. At the same time, the instability growth rates become smaller for the more asymmetric systems, see fig. 4.

Moreover, it is possible to observe a rather smooth and continuous transition from the trend observed at $\rho = 0.06\,\mathrm{fm}^{-3}$ (mechanical unstable region) to the trend observed at $\rho = 0.09\,\mathrm{fm}^{-3}$ (chemical unstable region), thus indicating that there is no qualitative change between the two kinds of instabilities. In fact they actually correspond to the same mechanism, the amplification of isoscalar-like fluctuations, with a significant chemical component (change of the concentration).

The conclusion is that the fast spinodal decomposition mechanism in neutron-rich matter will dynamically form more symmetric fragments surrounded by a less symmet-

ric gas. Some recent experimental observations from fragmentation reactions with neutron-rich nuclei at the Fermi energies seem to be in agreement with this result on the fragment isotopic content: nearly symmetric intermediate mass fragments (IMF) have been detected in connection to very neutron-rich light ions [13,14].

4 From bulk to neck fragmentation

4.1 Multifragmentation

Since dynamical instabilities are playing an essential role in the reaction dynamics at Fermi energies it is essential to employ a stochastic transport theory. An approach has been adopted based on microscopic transport equations of Boltzmann-Nordheim-Vlasov (BNV) type [28,32–35] where asymmetry effects are suitably accounted for [36,37] and the dynamics of fluctuations is included [38,39].

The transport equations, with Pauli blocking consistently evaluated, are integrated following a test particle evolution on a lattice [35,40,41]. A parametrization of free NN cross-sections is used, with isospin, energy and angular dependence. The same symmetry term is utilized even in the initialization, *i.e.* in the ground-state construction of two colliding nuclei.

In particular, we report on a study of the 50 AMeV collisions of the systems ^{124}Sn + ^{124}Sn ^{112}Sn + ^{112}Sn and ^{124}Sn + ^{112}Sn, [42], where data are available from NSCL-MSU experiments for fragment production. One can identify quite generally three main stages of the collision, as observed also from the density contour plot of a typical event at $b = 2$ fm displayed in fig. 7: 1) in the early compression stage, during the first 40–50 fm/c, the density in the central region can reach values around 1.2–1.3 normal density; 2) the expansion phase, up to 110–120 fm/c, brings the system to a low-density state. The physical conditions of density and temperature reached during this stage correspond to an unstable nuclear-matter phase; 3) in the further expansion fragmentation is observed.

According to stochastic mean-field simulations, the fragmentation mechanism can be understood in terms of the growth of density fluctuations in the presence of instabilities. The volume instabilities have time to develop through spinodal decomposition leading to the formation of a liquid phase in the fragments and a gas of nucleons and light clusters. As seen in the figure, the fragment formation process typically takes place up to a *freeze-out* time (around 260–280 fm/c). This time is well defined in the simulations since it is the time of saturation of the average number of excited primary fragments. The clusters are rather far apart with a negligible nuclear interaction left among them.

Guided by the density contour plots we can investigate the behaviour of some characteristic quantities which give information on the isospin dynamics in fragment formation. In fig. 8, we report as a function of time:

(a) *The mass A* in the liquid phase (solid line and dots) and gas phase (solid line and squares).

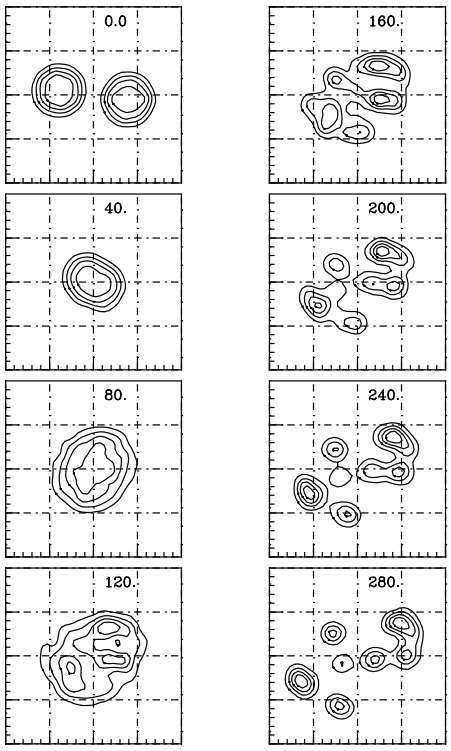

Fig. 7. Central $b = 2$ fm ^{124}Sn + ^{124}Sn collision at 50 AMeV: time evolution of the nucleon density projected on the reaction plane: approaching, compression and expansion phases. The times are written on each figure. The iso-density lines are plotted every 0.02 fm^{-3} starting from 0.02 fm^{-3}. The figure is taken from [42].

(b) *The asymmetry parameter* $I = (N - Z)/(N + Z)$ in the gas "central" (solid line and squares), gas total (dashed+squares), liquid "central" (solid+circles) and IMFs (clusters with $3 < Z < 15$, stars). The horizontal line indicates the initial average asymmetry. "Central" means a box of linear dimension 20 fm around the center of mass of the total system.

(c) *The mean fragment multiplicity* $Z \geq 3$ whose saturation defines the freeze-out time and configuration.

We also show some properties of the "primary" fragments in the *freeze-out configuration*:

(d) *The charge distribution probability P(Z)*,

(e) *The average asymmetry distribution* $I_{av}(Z)$ and

(f) *The fragment multiplicity distribution* $P(N)$ (normalized to 1).

For ^{124}Sn + ^{124}Sn we notice a neutron-dominated pre-equilibrium particle emission during the first 50 fm/c. The liquid phase becomes more symmetric during the compression and expansion. From the beginning of the fragment formation phase of the evolution, between 110 and 280 fm/c, we remark the peculiar trends of the liquid and gas phase asymmetry. In the "central region" the liquid asymmetry decreases while an *isospin burst* of the gas phase is observed. This behaviour is consistent with the

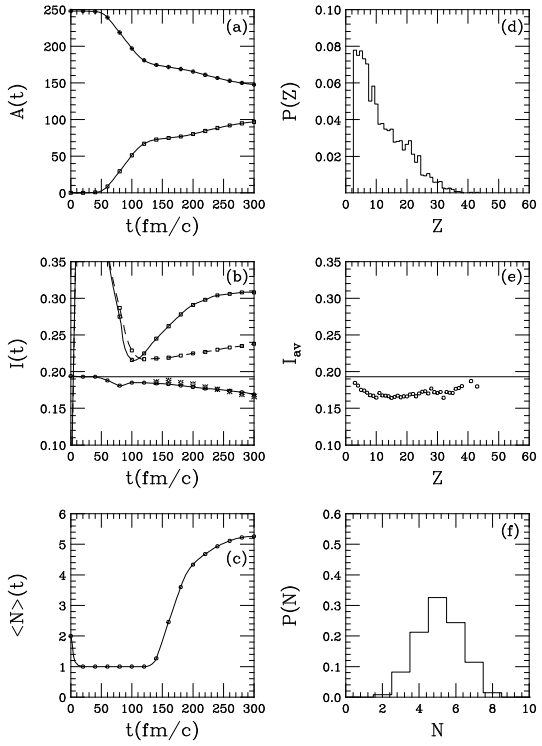

Fig. 8. The collision ^{124}Sn + ^{124}Sn at $b = 2$ fm: time evolution (left) and freeze-out properties (right), ASY-STIFF EOS. The figure is taken from [42].

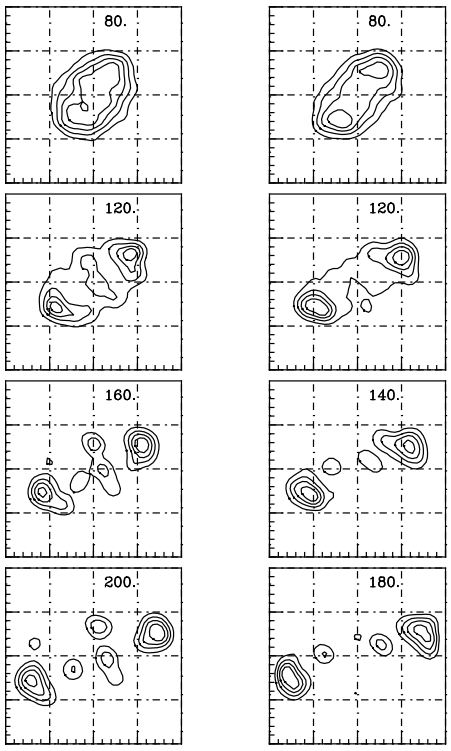

Fig. 9. ^{124}Sn + ^{124}Sn collision at 50 AMeV: time evolution of the nucleon density projected on the reaction plane. Left column: $b = 4$ fm. Right column: $b = 6$ fm. The figure is taken from [42].

kinetic spinodal mechanism in dilute asymmetric nuclear matter leading to the *isospin distillation* between the liquid and the gas phase.

The effects of this process are clearly seen in the IMF isospin content, in both cases lower than at the beginning of the spinodal decomposition, fig. 8(e). Opposite trends for fragments with charge above and below $Z \approx 15$ can be observed. For heavier products the average asymmetry increases with the charge, a Coulomb related effect. However, the asymmetry rises again for lighter fragments. This can be a result of the differences in density and isospin between the regions in which the fragments grow, due to the fact that not all of them form simultaneously, as shown in the density contour plot. Let us also observe that the charge distribution of primary fragments has a rapidly decreasing trend, typical of a multifragmentation process.

4.2 Neck fragmentation

Summarizing the main experimental observations, we enumerate the following features of a "dynamical" IMF production mechanism in semi-peripheral collisions:

1. An enhanced emission is localized in the mid-rapidity region, intermediate between projectile-like fragment (PLF) and target-like fragments (TLF) sources, especially for IMFs with charge Z from 3 to 15 units.

2. The IMFs relative velocity distributions with respect to PLF (or TLF) cannot be explained in terms of a pure Coulomb repulsion following a statistical decay. A high degree of decoupling from the PLF (TLF) is also invoked.

3. Anisotropic IMFs angular distributions are indicating preferential emission directions and an alignment tendency.

4. For charge asymmetric systems the light particles and IMF emissions keep track of a neutron enrichment process that takes place in the neck region.

A fully consistent physical picture of the processes that can reproduce observed characteristics is still a matter of debate and several physical phenomena can be envisaged, ranging from the formation of a transient neck-like structure that would break-up due to Rayleigh instabilities or through a fission-like process, to the statistical decay of a hot source, triggered by the proximity with PLF and TLF [43–45].

The development of a neck structure in the overlap region of the two colliding nuclei is evidenced in fig. 9. During the interaction time this zone heats and expands but remains in contact with the denser and colder regions of PLF and/or TLF. The surface/volume instabilities of a cylindrically shaped neck region and the fast leading motion of the PLF and TLF will play an important role in the fragmentation dynamics. We notice the superimposed motion of the PL and TL pre-fragments linked to

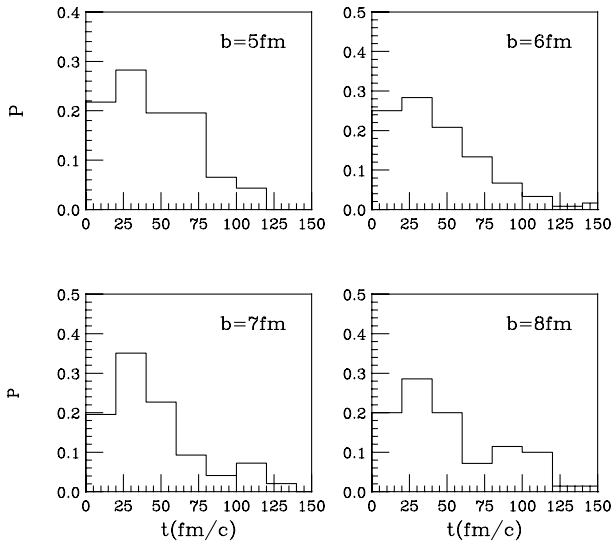

Fig. 10. The probability distribution of scission-to-scission time in the neck fragmentation for impact parameters from 5 to 8 fm. ^{124}Sn + ^{64}Ni at 35 AMeV and asystiff EOS. The figure is taken from [26].

the formation of a neck-like structure with a fast-changing geometry.

At the freeze-out time, with the neck rupture at about 140 fm/c, intermediate mass fragments are produced in the mid-rapidity zone. In some events fragments form very early while, in others, they can remain for a longer time attached to the leading PLFs or TLFs. A transition behavior between multifragmentation and neck fragmentation is observed at $b = 4$ fm.

From the simulations we can extract an interesting information on the time scale of the Neck-IMF production. In fig. 10 we show, for different impact parameters, the probability distribution of the time interval between the instant of the first separation of the dinuclear system and the moment when a Neck-IMF is identified (scission-to-scission time). A large part of the Neck-IMFs are formed in short time intervals, within 50 fm/c.

Finally, we would like to remark that the neck fragmentation shows a dependence on the nucleon-nucleon cross-sections and the EOS compressibility. The latter point is particularly interesting since it seems to indicate the relevance of volume instabilities even for the dynamics of the neck. This appears consistent with the short time scales shown before, see also the discussion in ref. [46].

5 Conclusions

In this work we investigated several properties of the asymmetric nuclear matter in the low-density region of phase diagram. The thermodynamical and dynamical analysis was based on Landau theory of Fermi liquid extended to binary systems. It was concluded that:

- at low densities, of interest for the nuclear liquid-gas phase transition, the asymmetric nuclear matter can be characterized by a unique spinodal region, defined by the instability against isoscalar-like fluctuations; inside this we can identify the region where the system manifests mechanical instability and chemical instability, respectively;
- the physical meaning of thermodynamical chemical and mechanical instabilities should be related to the relative strengths of the interactions among the different species.
- everywhere in this density region the system is stable against the isovector-like fluctuations related to a tendency for species separation.
- at larger initial asymmetries the development of the spinodal instabilities is slower and a depletion of the maximum of the growth rate takes place. A decrease of the wave number corresponding to the maximum growth rate was deduced. Also the Coulomb force causes an overall decrease of growth rates. In this case the wave vector should exceed a threshold value in order to observe the instabilities.
- during the time development of the spinodal instabilities in ANM the fragment formation is accompanied by the isospin distillation leading to a more symmetric liquid phase and more neutron-rich gas phase.

We have made a connection of these features with isospin transport properties in simulations of fragmentation reactions based on stochastic BNV transport models. The presence and the role of the instabilities along the reaction dynamics in bulk fragmentation and neck fragmentation were discussed.

The results discussed here refer to the formation processes of primary fragments. *i.e.* at the freeze-out time. We explored the possibility that IMF appear as a result of a mechanism that initially started as spinodal decomposition triggered by isoscalar-like instabilities. These fragments are excited, and the subsequent statistical decay will certainly modify the signal. Therefore, it is important to search for various observables still keeping informations about the early stages of the fragments formation, for example those related to the kinematical properties (velocity distributions, angular distributions) and correlations between these observables and isospin content.

Moreover, the neck dynamics and corresponding isospin transport shows distinctive features related to the interplay between volume and surface instabilities. These should be better clarified in the future since they can contribute to a proper understanding of intermediate mass fragment production at Fermi energies.

V.B. acknowledges support of the Romanian Ministry for Education and Research for this work under the contract No. CEx-05-D10-02.

References

1. M. Barranco, J.R. Buchler, Phys. Rev. C **22**, 1729 (1980).
2. L.D. Landau, Sov. Phys. JETP **5**, 101 (1957).

3. A.B. Migdal, *Theory of finite Fermi systems and applications to atomic nuclei* (Wiley & Sons, N.Y., 1967).
4. G. Baym, C.J. Pethick, in *The Physics of Liquid and Solid Helium*, edited by K.H. Bennemann, J.B. Ketterson, Vol. **2** (Wiley, New-York, 1978) p. 1.
5. C.J. Pethick, D.G. Ravenhall, Ann. Phys. (N.Y.) **183**, 131 (1988).
6. N. Iwamoto, C.J. Pethick, Phys. Rev. D **25**, 313 (1982).
7. L.D. Landau, E.M. Lifshitz, *Statistical Physics* (Pergamonn Press, 1989) p. 288.
8. H. Müller, B.D. Serot, Phys. Rev. C **52**, 2072 (1995).
9. B.-A. Li, C.M. Ko, Nucl. Phys. A **618**, 498 (1997).
10. V. Baran, M. Colonna, M. Di Toro, V.G reco, Phys. Rev. Lett. **86**, 4492 (2001).
11. M. Colonna, M. Di Toro, A.B. Larionov, Phys. Lett. B **428**, 1 (1998).
12. V. Baran, M. Colonna, M. Di Toro, A.B. Larionov, Nucl. Phys. A **632**, 287 (1998).
13. H.S. Xu *et al.*, Phys. Rev. Lett. **85**, 716 (2000).
14. S.J. Yennello, *Proceedings of the International School-Seminar on Heavy Ion Physics*, edited by Yu.Ts. Oganessian (World Scientific, 1997).
15. J. Margueron, Ph. Chomaz, Phys. Rev. C **67**, 041602(R) (2003).
16. B. Liu, V. Greco, V. Baran, M. Colonna, M. Di Toro, Phys. Rev. C **65**, 045201 (2002).
17. S.S. Avancini, L. Brito, D.P. Menezes, C. Providencia, Phys. Rev. C **70**, 015203 (2004).
18. P. Haensel, Nucl. Phys. A **301**, 53 (1978).
19. F. Matera, V.Yu. Denisov, Phys. Rev. C **49**, 2816 (1994).
20. G. Baym, H.A. Bethe, C.J. Pethick, Nucl. Phys. A **175**, 225 (1971).
21. H. Krivine, J. Treiner, O. Bohigas, Nucl. Phys. A **336**, 155 (1990).
22. M. Colonna, Ph. Chomaz, Phys. Rev. C **49**, 1908 (1994).
23. M. Colonna, Ph. Chomaz, J. Randrup, Nucl. Phys. A **567**, 637 (1994).
24. Ph. Chomaz, M. Colonna, J. Randrup, Phys. Rep. **389**, 263 (2004).
25. M. Colonna, Ph. Chomaz, S. Ayik, V. Greco, Phys. Rev. Lett. **88**, 122701 (2002).
26. V. Baran, M. Colonna, V. Greco, M. Di Toro, Phys. Rep. **410**, 335 (2005).
27. B.-A. Li, A.T. Sustich, M. Tilley, B. Zhang, Nucl. Phys. A **699**, 493 (2002).
28. Ch. Grégoire *et al.*, Nucl. Phys. A **465**, 315 (1987).
29. A. Bonasera, F. Gulminelli, J. Molitoris, Phys. Rep. **243**, (1994).
30. V. Baran, A. Bonasera, M. Colonna, M. Di Toro, A. Guarnera, Prog. Part. Nucl. Phys. **38**, 263 (1997).
31. M. Colonna, M. Di Toro, A. Guarnera, Nucl. Phys. A **580**, 312 (1994).
32. G.F. Bertsch, S. Das Gupta, Phys. Rep. **160**, 189 (1988).
33. A. Bonasera *et al.*, Phys. Rep. **244**, 1 (1994).
34. A. Bonasera, G.F. Burgio, M. Di Toro, Phys. Lett. B **221**, 233 (1989).
35. TWINGO code: A. Guarnera PhD Thesis, University Caen (1996).
36. M. Colonna, M. Di Toro, G. Fabbri, S. Maccarone, Phys. Rev. C **57**, 1410 (1998).
37. L. Scalone, M. Colonna, M. Di Toro, Phys. Lett. B **461**, 9 (1999).
38. M. Di Toro *et al.*, Progr. Part. Nucl. Phys. **42**, 125 (1999).
39. M. Colonna *et al.*, Nucl. Phys. A **642**, 449 (1998).
40. A. Guarnera, M. Colonna, Ph. Chomaz, Phys. Lett. B **373**, 267 (1996).
41. V. Greco, Diploma Thesis (1997); V. Greco, A. Guarnera, M. Colonna, M. Di Toro, Phys. Rev. C **59**, 810 (1999).
42. V. Baran *et al.*, Nucl. Phys. A **703**, 603 (2002).
43. U. Brosa, S. Grossman, A. Muller, Phys. Rep. **197**, 167 (1990).
44. J. Lukasik *et al.*, Phys. Lett. B **566**, 76 (2003).
45. A.S. Botvina *et al.*, Phys. Rev. C **59**, 3444 (1999).
46. V. Baran, M. Colonna, M. Di Toro, Nucl. Phys. A **730**, 329 (2004).